

# Thermal Runaway of Chemical Reactors: An Experimental, Modeling, and Machine-Learning Investigation

Published as part of *Industrial & Engineering Chemistry Research special issue* “2025 NASCRE-5: Breaking Barriers for a Sustainable Future”.

Tobias K. Misicko,<sup>†</sup> Joaquin Herrero,<sup>†</sup> Jacob C. Robinson,<sup>†</sup> Daniela S. Mainardi, and Yang Xiao\*



Cite This: *Ind. Eng. Chem. Res.* 2026, 65, 2057–2070



Read Online

ACCESS |



Metrics & More

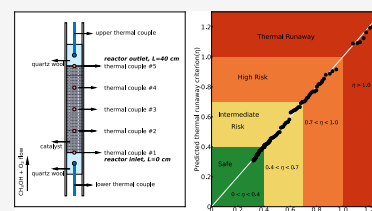


Article Recommendations



Supporting Information

**ABSTRACT:** Thermal runaway of chemical reactors remains a central challenge in chemical process safety because small imbalances between heat generation and removal can trigger rapid temperature escalation. In this contribution, we combine mechanistic modeling, targeted experiments, and data-driven tools to predict both the onset and intensity of chemical reactor runaway, demonstrated here for batch and fixed-bed systems and formulated to be extensible to other reactor types and reaction networks. Experimentally, we investigate selective methanol oxidation over Pt–Bi/activated carbon in a fixed-bed reactor and measure axial temperature profiles under varied feed temperature and oxygen concentration. A five-reaction pseudohomogeneous plug-flow model, coupled with sensitivity analysis of  $T_{\max}$  identifies critical operating thresholds and clarifies how Bi promotion suppresses highly exothermic  $\text{CO}_2$  pathways, widening the safe operating window. To generalize prediction beyond single-reaction systems, we formulate data sets of dimensionless groups ( $\gamma$ ,  $B$ ,  $Da$ ,  $St$ ,  $\psi$ ) for batch and flow reactors and introduce a kinetic weighting factor  $\sigma_n$  to map multireaction mechanisms onto an effective parameter space. Logistic Regression, Random Forest, and Support Vector models are trained and validated on literature data (acetic anhydride hydrolysis, batch) and our fixed-bed experiments (methanol oxidation), with Random Forest providing the highest accuracy and the lowest miss rate (false negatives) for classifying runaway onset. We propose a continuous, ML-informed criticality metric,  $\eta$ , which aggregates feature importance with proximity to classical critical values to quantify “how close” a system is to runaway. This unified framework links mechanistic insight with fast, reliable prediction, enabling safer operating envelopes, catalyst-informed mitigation strategies, and practical early warning diagnostics for industrial reactors.



## 1. INTRODUCTION

Thermal runaway of chemical reactors is characterized by a repeated cycle where there is a progressive increase in temperature caused by an accumulation of heat due to insufficient cooling. This temperature increase accelerates the reaction rate of a strongly exothermic reaction, leading to further heat release and eventually a destructive outcome such as a thermal explosion. In industrial practice, such accidents have been reported in polymerization, nitration, and hydrogenation systems, often resulting in severe casualties, large-scale equipment damage, and significant financial losses.<sup>1,2</sup> The underlying hazard originates from the nonlinear coupling between chemical kinetics and reactor heat transfer, where even a minor imbalance between heat generation and removal can destabilize reactor operation. Factors such as high reactant loading, poor mixing, or cooling failure can accelerate this progression, highlighting the narrow margin between stable operation and runaway. Because of these risks, understanding and preventing thermal runaway has long been a central issue in chemical reaction engineering, driving research into detection, modeling, and control strategies for safe operation and loss prevention across the chemical and related industries.

The ability to accurately model and predict the onset of thermal reactor runaway is paramount for ensuring safe operation, and numerous approaches have been proposed over the past century. Following Semenov’s foundational theory,<sup>3</sup> several thermal runaway criteria were developed to capture instability boundaries. The Thomas–Bowes (TB)<sup>4</sup> and Adler–Enig (AE)<sup>5</sup> criteria identify runaway through the occurrence of a positive second-order derivative prior to the maximum temperature in either the temperature–time or temperature–conversion domains. The Morbidelli–Varma (MV) criterion<sup>6–11</sup> and the Henning–Perez (HP) criterion<sup>12</sup> instead locate the runaway boundary within regions highly sensitive to small parameter variations. Strozzini and Zaldivar introduced the divergence (SZ) criterion,<sup>13–17</sup> which characterizes runaway by analyzing chaotic attractors and the

**Received:** September 29, 2025

**Revised:** December 26, 2025

**Accepted:** January 8, 2026

**Published:** January 20, 2026



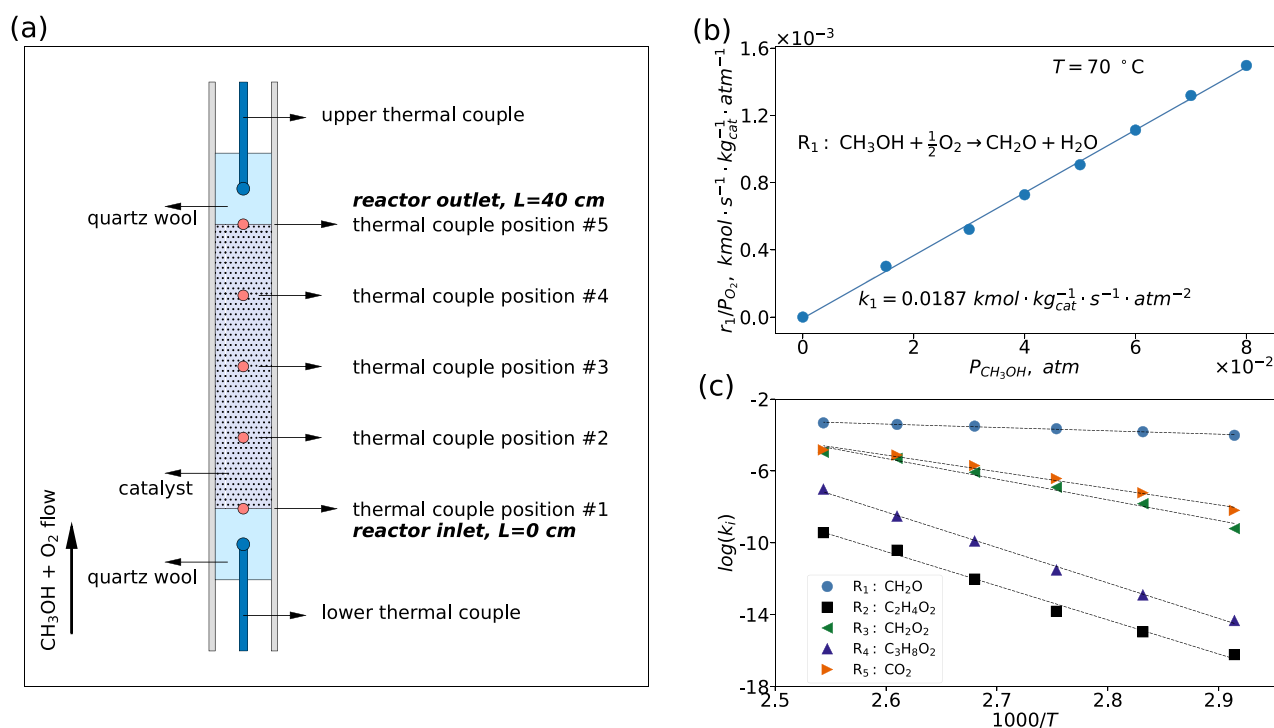


**Figure 1.** Kinetics investigation: (a) Schematic of the fixed-bed reactor apparatus fabricated from 316 L stainless steel tubing with outer and inner diameters of 12.7 mm and 11.7 mm, respectively, and an overall length of 400 mm. Thermocouples in the catalyst bed section were positioned at 10 mm intervals along the axial direction. (b) Reaction rate fit for step R<sub>1</sub> at  $T_0 = 343$  K using 0.02 g of packed catalyst and a methanol feed rate of 0.6 mL/h, showing conversion of methanol to formaldehyde at varying CH<sub>3</sub>OH partial pressures. (c) Arrhenius plots for reaction steps R<sub>1</sub>–R<sub>5</sub> under standard operating conditions, with temperatures varied between 343–393 K using 0.02 g of packed catalyst, an O<sub>2</sub> feed at 50% of the stoichiometric value, and a CH<sub>3</sub>OH:O<sub>2</sub> molar ratio of 4:1.

expansion or contraction of phase-space volume elements. Although these classical criteria differ in formulation, they generally converge on similar predictions of the runaway limit.<sup>18</sup> More recent developments have refined these approaches. Adrover et al. proposed a method based on tangential stretching rates along system trajectories, where instabilities indicate runaway; this method successfully estimated explosion limits in the H<sub>2</sub>–O<sub>2</sub> system.<sup>19</sup> Jiang et al. later introduced a modified divergence criterion based on the Jacobian matrix, where critical conditions are identified when the Jacobian trace reaches a maximum; the predictions showed good agreement with the MV criterion in assessing methyl nitrate decomposition.<sup>20</sup> Building on existing frameworks, Kummer and Varga developed two hybrid criteria by combining critical equation terms, which proved effective in optimizing feed trajectories for fed-batch 2-octanone oxidation reactors.<sup>21,22</sup>

In fact, whatever criteria are applied to estimate the thermal runaway boundary, all require time-consuming computations and sophisticated mathematical thresholds, where numerous parameters such as the properties of reactants, the dimensions of the reactor, the temperature, and the flow rate of coolant are required for the full description of a reactor. In addition, multiple ordinary differential equations (ODEs) must be solved to obtain the runaway boundary. Although these methods are feasible for a limited number of cases, the estimation of thermal runaway for a great number of reactors becomes mathematically demanding, a situation that is increasingly common in today's large chemical plants. Therefore, beyond relying solely on classical models, there is a pressing need for pragmatic alternatives that can rapidly and

precisely evaluate thermal runaway. Machine learning (ML) represents an ideal candidate due to the inherent complexity of the mathematical modeling of chemical reactor runaway. ML has transformed engineering by converting millions of data points into actionable information, and it has emerged as a robust tool to address multidimensional problems in chemical engineering, including catalyst design,<sup>23</sup> crystal identification,<sup>24</sup> activity coefficient prediction,<sup>25</sup> and fault diagnosis of chemical processes.<sup>26</sup> However, the application of ML to classify thermal reactor runaway remains limited. In one example, Varga et al. utilized a Decision Tree (DT) algorithm to distinguish between runaway and nonrunaway scenarios in a fixed-bed reactor, developing a tool capable of forecasting runaway events.<sup>27</sup> Similarly, Kummer et al. employed genetic programming to generate equations that could accurately indicate runaway in both continuously stirred tank reactors (CSTRs) and batch reactors.<sup>21</sup> Despite these important advances, there is still no generalized framework capable of identifying thermal reactor runaway across diverse reactor configurations and multiple-reaction mechanisms.

In our prior research, Pt–Bi bimetallic catalysts were investigated for the catalytic conversion of glycerol to 1,3-dihydroxyacetone,<sup>28,29</sup> the deoxygenation of guaiacol using methane,<sup>30,31</sup> and the nonoxidative coupling of methane,<sup>32</sup> with emphasis on parametric sensitivity, catalyst design, and reactor safety. Building on this foundation, the present work develops a transferable machine-learning (ML) framework to evaluate reactor thermal behavior, demonstrated on batch and fixed-bed configurations. Several algorithms, including Logistic Regression (LR), Ridge Regression (RR), Random Forest (RF), and Support Vector Machine (SVM), were trained and

validated, beginning with literature data on acetic anhydride hydrolysis reported by Haldar and Rao.<sup>33</sup> To further demonstrate applicability, the selective oxidation of methanol to formaldehyde was studied experimentally, and the resulting data were used to establish a kinetic model. This model enabled the generation of a data set of runaway instances in a packed-bed reactor, which was then analyzed using ML. From the feature importance analysis of the RF algorithm, a new ML-based criterion ( $\eta$ ) is proposed to predict the extent of reactor criticality, and its potential applications for practical reactor safety evaluation are discussed. To the best of our knowledge, this study is the first to integrate reported literature data, new fixed-bed experimental measurements, and classical mechanistic modeling within a unified machine-learning framework to predict both the onset and the extent of thermal runaway in reacting-flow systems. Prior machine-learning efforts related to thermal runaway have focused primarily on battery cells and energy-storage materials rather than catalytic reactors, and no previous work has combined mechanistic criteria, experimental validation, and ML-based criticality metrics as demonstrated here. This integrated approach therefore represents a distinct and innovative contribution.

## 2. METHODS

### 2.1. Catalyst Synthesis and Materials

Hexachloroplatinic acid and bismuth(III) chloride (both >99.9% metals basis, Sigma-Aldrich) were used as Pt and Bi precursors, respectively. Activated carbon (AC, 80–120 mesh, Norit Americas, Inc.) served as the catalyst support. Calibration compounds—including methanol (99%), formaldehyde (37 wt % solution with 7–8% methanol as stabilizer in water), methyl formate (97%), dimethoxymethane (98%), and formic acid (97%)—were purchased from Alfa Aesar. The following gas purities were used in this study: Ar (99.999%), CO<sub>2</sub> (99.99%), H<sub>2</sub> (99.999%), He (99.98%), N<sub>2</sub> (99.999%), and O<sub>2</sub> (99.98%). Following our previous procedure,<sup>32,34</sup> Pt–Bi catalysts were synthesized by the wet impregnation method, with Pt loaded first followed by Bi. For simplicity, the catalyst descriptions in subsequent sections omit explicit reference to the AC support, since it was the only support material used, and all Pt and Bi loadings are reported on a weight (wt) basis.

### 2.2. Catalyst Tests and Measurements of Kinetics and Reactor Temperatures

Catalytic performance tests were conducted in a fixed-bed reactor, as shown in Figure 1 (a). Prior to tests, the packed catalysts were reduced at 723 K for 4 h under a H<sub>2</sub>–N<sub>2</sub> gas mixture (H<sub>2</sub>:N<sub>2</sub> = 1:2). The reactor was then purged with nitrogen for 15 min. The standard operating conditions were: 343 K, 1 atm, 0.02 g catalyst, methanol feed rate of 0.6 mL/h (liquid, at room temperature), preheated to 343 K before entering the reactor, and a total gas flow rate of 100 mL/min (corresponding to 6% CH<sub>3</sub>OH, 1.5% O<sub>2</sub>, and 92.5% N<sub>2</sub>). These feed rates corresponded to a molar ratio of 4:1 between CH<sub>3</sub>OH and O<sub>2</sub>, i.e., using 50% of the stoichiometric O<sub>2</sub> as described later in eq 4. As noted in our prior work,<sup>34</sup> a substoichiometric O<sub>2</sub> feed was used to suppress overoxidation of products (e.g., formic acid, CO<sub>2</sub>). An Agilent 6890 gas chromatography (GC) system equipped with a DB-1701 column (30 m × 0.25 mm) and a flame ionization detector (FID) was used for quantitative analysis of liquid products. The gaseous reactor effluent was analyzed using an Agilent 3000A micro-GC equipped with two columns (Column A:

Molsieve 5A, 10 m × 0.32 mm; Column B: Plot U, 8 m × 0.32 mm) and two thermal conductivity detectors (TCDs). All catalytic performance data were collected at 0.5 h time-on-stream (TOS). Blank tests using the AC support were carried out under identical operating conditions, with methanol conversion always less than 0.3%. Carbon mass balances were consistently within 94 ± 2%.

For axial temperature profile measurements, two K-type thermocouples were inserted from both ends of the reactor. Temperatures at four axial positions (L = 10, 20, 30, and 40 cm) were measured in duplicate experiments, with L = 0 cm considered as the feed temperature. The reactor bed length was maintained at 40 cm by mixing the active catalyst with ~ 0.50 g of inert AC to ensure uniform packing. The reactor tube was immersed in a constant-temperature water bath (T<sub>c</sub> = 343 K). All experiments were repeated at least twice, with repeatability confirmed and deviations within 2% for all quantitative analyses.

### 2.3. Model Development of Reaction Kinetics and Fixed-Bed Reactor

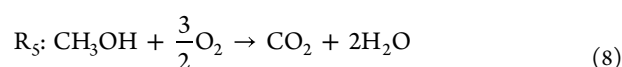
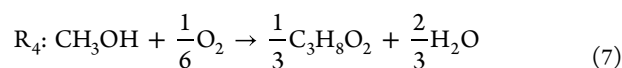
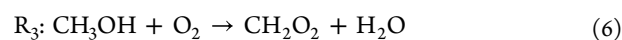
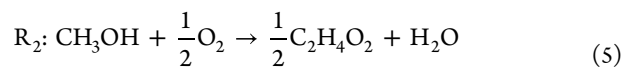
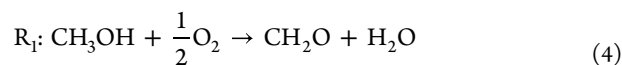
Several key performance metrics, including methanol conversion, product selectivity, and yield, are defined as follows:

$$\text{Methanol conversion} = \frac{\text{mol of reacted methanol}}{\text{mol of methanol feed}} \quad (1)$$

$$\text{Product selectivity} = \frac{\text{mol of formed product}}{\text{mol of reacted methanol}} \quad (2)$$

$$\text{Product yield} = \frac{\text{mol of formed product}}{\text{mol of methanol feed}} \quad (3)$$

Consistent with our prior study,<sup>34</sup> the target product was formaldehyde (CH<sub>2</sub>O), and four byproducts were typically observed: methyl formate (C<sub>2</sub>H<sub>4</sub>O<sub>2</sub>), formic acid (CH<sub>2</sub>O<sub>2</sub>), dimethoxymethane (C<sub>3</sub>H<sub>8</sub>O<sub>2</sub>), and carbon dioxide (CO<sub>2</sub>). Because methanol conversion remained low (<10%) under thermally stable conditions, only five parallel reactions—each initiated from methanol and oxygen—were considered in the kinetic model, as shown in eqs 4–(8). Further reactions of products (e.g., oxidation of CH<sub>2</sub>O to CO<sub>2</sub>) were not included for simplification of the reaction network. Because all kinetic parameters were measured under low-conversion, nonthermal conditions where methanol conversion remained below 10%, the simplified five-reaction mechanism is an appropriate and deliberate choice for thermal-safety analysis in this regime; deeper secondary oxidation pathways ultimately converge to the highly exothermic CO<sub>2</sub>-forming reaction already represented in R<sub>5</sub>, and extending the mechanism to include detailed higher-order oxidation sequences is a valuable direction for future work.



The kinetics of these reactions follow a power-law rate form, as expressed in eqs 9–(10):

$$r_i = kP_{\text{CH}_3\text{OH}}^{n_{(i,1)}}P_{\text{O}_2}^{n_{(i,2)}}; \quad i = 1-5 \quad (9)$$

$$P_j = \frac{P_0}{F_0}F_j; \quad j = 1-9 \quad (10)$$

For the reactor model, a one-dimensional pseudohomogeneous plug-flow formulation was employed, as described by eqs 11–(15):

$$\frac{dF_j}{dW} = \sum_{i=1}^5 \alpha_{(i,j)}r_i; \quad j = 1-9 \quad (11)$$

$$c_p F \frac{dT}{dW} = \sum_{i=1}^5 (-\Delta H_{r,i})r_i - \frac{4U}{d_t \rho_{\text{cat}}}(T - T_c) \quad (12)$$

$$c_p = \sum_{j=1}^9 \frac{P_j}{P_{\text{total}}}c_{p,j} \quad (13)$$

$$c_{p,j} = C_{1j} + C_{2j} \left( \frac{\frac{C_{sj}}{T}}{\sinh\left(\frac{C_{sj}}{T}\right)} \right)^2 + C_{4j} \left( \frac{\frac{C_{sj}}{T}}{\cosh\left(\frac{C_{sj}}{T}\right)} \right)^2 \text{ for } C_{6j} < T < C_{7j} \quad (14)$$

$$\frac{1}{U} = \frac{1}{\alpha_i} + \frac{d}{\lambda} \frac{A_b}{A_m} + \frac{1}{\alpha_u} \frac{A_b}{A_u} \quad (15)$$

The bed-side heat-transfer coefficient  $\alpha_i$  was obtained from the Wakao–Funazkri packed-bed correlation, using the reactor inner diameter  $D_i$  as the characteristic length and the thermal conductivity of the  $\text{N}_2$ -rich reactant mixture ( $\lambda_g \approx 0.030 \text{ W m}^{-1} \text{ K}^{-1}$  at 400 K), whereas the wall-side coefficient  $\alpha_u$  was computed from an external forced-convection correlation for air flowing over a cylinder, with the outer diameter  $D_o$  as the characteristic length and  $\lambda_{\text{air}} \approx 0.031 \text{ W m}^{-1} \text{ K}^{-1}$ ; in eq 15, the wall term uses the stainless-steel conductivity  $\lambda_s \approx 16 \text{ W m}^{-1} \text{ K}^{-1}$ . In eqs 9–15,  $i = 1 - 5$  corresponds to the five reaction steps ( $\text{R}_1$ – $\text{R}_5$ ), and  $j = 1 - 9$  corresponds to the species  $\text{CH}_3\text{OH}$ ,  $\text{O}_2$ ,  $\text{CH}_2\text{O}$ ,  $\text{C}_2\text{H}_4\text{O}_2$ ,  $\text{CH}_2\text{O}_2$ ,  $\text{C}_3\text{H}_8\text{O}_2$ ,  $\text{CO}_2$ ,  $\text{H}_2\text{O}$ , and  $\text{N}_2$  (inert carrier gas).

Following eq 14, the heat capacity of each pure component was obtained using DIPPR eq 107,<sup>35</sup> with parameter values listed in Table S1. The mixture heat capacity was calculated using the mixing rule in eq 13. The overall wall heat transfer coefficient ( $U$ ) was estimated using eq 15.<sup>36</sup> The overall heat-transfer coefficient  $U$  is treated in this work as an effective, approximate parameter that represents the overall heat-removal capability of the experimental setup. Because detailed heat-transfer coefficients and temperature-dependent transport properties were not independently measured, the model is intended to capture trends in axial temperature evolution and to identify the onset and proximity of thermal runaway, rather than to provide high-fidelity prediction of absolute hotspot magnitudes.

The initial conditions were

$$F_i = F_{i,0}, \quad T = T_0 \text{ when } W = 0 \quad (16)$$

The above ODE system was solved numerically using the `zvode` solver from `scipy.integrate` (the SciPy package, [www.scipy.org](http://www.scipy.org), employing the BDF (backward

differentiation formula) method. Step sizes of 100, 200, and 500 were tested along the reactor length. The step-size sensitivity was evaluated using the steep near-critical temperature profile at an inlet temperature of  $T_0 = 403 \text{ K}$ , which provides the largest axial temperature gradients and therefore the most stringent test of numerical resolution. It was found that 200 and 500 steps gave essentially identical results (e.g., reactor temperature up to five significant figures), and therefore a 200-step size was employed in all calculations.

To quantify the sensitivity of the maximum reactor temperature ( $T_{\text{max}}$ ) to changes in operating conditions, sensitivity coefficients were defined with respect to the inlet temperature ( $T_0$ ) and oxygen partial pressure ( $P_{\text{O}_2}$ ), as shown in eqs 17–(18). These dimensionless coefficients normalize the rate of change of  $T_{\text{max}}$  with respect to each parameter, thereby allowing a direct comparison of their relative influence on runaway behavior. Specifically, eq 17 evaluates the effect of perturbations in  $T_0$  on  $T_{\text{max}}$  while eq 18 captures the impact of changes in  $P_{\text{O}_2}$ . Larger values of the sensitivity coefficients indicate that small deviations in the corresponding parameter strongly amplify the maximum temperature, highlighting critical conditions for thermal runaway.

$$S(T_{\text{max}}; T_0) = \frac{T_0}{T_{\text{max}}} \cdot s(T_{\text{max}}; T_0) = \frac{T_0}{T_{\text{max}}} \cdot \frac{\partial T_{\text{max}}}{\partial T_0} \quad (17)$$

$$S(T_{\text{max}}; P_{\text{O}_2}) = \frac{P_{\text{O}_2}}{T_{\text{max}}} \cdot s(T_{\text{max}}; P_{\text{O}_2}) = \frac{P_{\text{O}_2}}{T_{\text{max}}} \cdot \frac{\partial T_{\text{max}}}{\partial P_{\text{O}_2}} \quad (18)$$

#### 2.4. Model Development of Machine-Learning Criterion for Thermal Runaway Prediction

Thermal runaway data from industry is scarce and usually limited to specific reactions or reactor types, as operating close to the runaway boundary poses significant risks. To address this limitation, we combined two sources of data: 200 experimental cases of catalytic acetic anhydride hydrolysis reported in the literature,<sup>33</sup> and 200 cases from our own methanol oxidation experiments. The combined data set is expressed as

$$\text{Dataset} = [\gamma, \psi, B, Da, St, R, \eta]$$

Here,  $[\gamma, \psi, B, Da, St]$  represent the matrix of dimensionless parameters— dimensionless activation energy ( $\gamma$ ), Semenov number ( $\psi$ ), dimensionless heat of reaction ( $B$ ), Damköhler number ( $Da$ ), and Stanton number ( $St$ )— which describe the intrinsic properties of the reaction and reactor systems (detailed in the Supporting Information). These quantities serve as the features for the ML models. The variable  $R$  denotes the onset of thermal runaway ( $R = 0$  for nonrunaway,  $R = 1$  for runaway), and  $\eta$  denotes the extent of criticality, discussed further in the following sections.

According to Varma et al.,<sup>18</sup> batch reactors can be fully characterized by  $[\gamma, \psi, B]$ , while plug-flow reactors (PFRs) are characterized by  $[\gamma, B, Da, St]$ . Dimensionless parameters not applicable to a given reactor type are set to zero (e.g.,  $Da$  and  $St$  for batch reactors,  $\psi$  for PFRs). Thus, the feature space is  $[\gamma, \psi, B, 0, 0]$  for batch reactors and  $[\gamma, 0, B, Da, St]$  for PFRs. To reduce model complexity, ambient temperature ( $\theta_a$  for batch reactors) and coolant temperature ( $\theta_{co}$  for PFRs) were set to zero. For each reactor type, 5,000 synthetic data sets were generated using the Adler–Enig (AE) and Henning–Perez (HP) criteria. The AE criterion was used for acetic anhydride

hydrolysis (batch reactor), and the HP criterion was applied to methanol oxidation (packed-bed reactor). The AE and HP criteria were chosen for the batch and fixed-bed reactors, respectively, because they are the standard onset definitions for lumped, spatially uniform systems and for spatially distributed packed-bed systems, and therefore reflect the appropriate instability physics for each reactor type. A detailed description of the synthetic data-generation workflow, including sampling of operating parameters, numerical solution of the governing equations, application of AE and HP criteria to assign stability labels, and assembly of the dimensionless input matrix, is provided in the [Supporting Information](#) to ensure full transparency and reproducibility.

The data sets were partitioned into training, validation, and testing subsets. Experimental data were reserved exclusively for testing, while generated data sets were split into two-thirds training and one-third validation. The final split is summarized as

(5,000 Generated + 200 Experimental)

Training: Validation: Testing = 3,333: 1,667: 200

Machine-learning modeling and evaluation were carried out in Python, using `scikit-learn` for algorithm development, `pandas` for data handling, and `scipy` for numerical operations. ML models were validated against literature data for batch acetic anhydride hydrolysis<sup>33</sup> and then applied to our packed-bed reactor methanol oxidation experiments. The batch reactor ML model was trained and validated using the AE-labeled batch data set, and the packed-bed reactor ML model was trained and validated using the HP-labeled packed-bed data set; the two reactors were analyzed independently, and no ML model was ever applied across reactor types. Predicting the onset of thermal runaway was formulated as a classification problem. Three algorithms were evaluated: Logistic Regression (LR), Random Forest (RF, with 150 trees), and Support Vector Machine (SVM). The model features were  $[\gamma, \psi, B, Da, St]$ , with output  $R$ . Hyperparameters were optimized by random search ([Tables S5–S8](#)). Performance was assessed using accuracy and miss rate (false negative rate). Each model was executed 50 times, and mean values were reported. Accuracy and miss rate are defined as

$$\text{Accuracy} = \frac{\text{TP} + \text{TN}}{\text{TP} + \text{TN} + \text{FP} + \text{FN}}$$

$$\text{Miss Rate} = \frac{\text{FN}}{\text{FN} + \text{TP}}$$

where TP, TN, FP, and FN denote true positives, true negatives, false positives, and false negatives, respectively. The goal is to maximize accuracy while minimizing miss rate, with particular emphasis on avoiding false negatives (misclassifying runaway as nonrunaway). To construct the test data sets, dimensionless parameters  $[\gamma, \psi, B, Da, St]$  were calculated from experimental conditions (initial temperature and other physicochemical properties, see [SI](#)). Although runaway onset values were available from the literature<sup>33</sup> and our own experiments, they were revalidated using classical runaway criteria to ensure consistency. A key limitation of classical runaway criteria is that they were originally formulated for single reactions, whereas our methanol oxidation system involves five parallel reactions. To account for this, we introduced a normalization parameter  $\sigma_n$  that weighs the

kinetic contribution of each reaction step, as defined in [Eqs. 19–24](#).

$$\sigma_n = \frac{k_n(T_i)}{k_1(T_i) + k_2(T_i) + k_3(T_i) + k_4(T_i) + k_5(T_i)} \quad (19)$$

$$\gamma = \sum_{n=1}^5 \gamma_n \cdot \sigma_n \quad (20)$$

$$B = \sum_{n=1}^5 B_n \cdot \sigma_n \quad (21)$$

$$Da = \sum_{n=1}^5 Da_n \cdot \sigma_n \quad (22)$$

$$St = \sum_{n=1}^5 St_n \cdot \sigma_n \quad (23)$$

$$\psi = \sum_{n=1}^5 \psi_n \cdot \sigma_n \quad (24)$$

All these dimensionless groups are defined in [Supporting Information](#). Once the normalized experimental data sets were established, generated data sets were calculated in the same way, covering the parameter ranges summarized in [Table 1](#).

**Table 1. Parameter Ranges Used for Generating Synthetic Datasets for Batch and Packed-Bed Reactors (PBR)**

| Parameter | Batch   | PBR    |
|-----------|---------|--------|
| $\gamma$  | 5–40    | 1–30   |
| $B$       | 5–20    | 0.25–2 |
| $Da$      | 0       | 0.5–4  |
| $St$      | 0       | 0.4–1  |
| $\psi$    | 0.2–2.1 | 0      |

Both experimental and generated data sets were used to train and test the ML classification models (LR, RF, and SVM). To quantify the extent of criticality as a measure of practical runaway risk, we propose a new ML-based criterion  $\eta$ , defined as

$$\text{Batch Reactor: } \eta = \sum_{j=1}^3 \omega_{P_j} \frac{P_j}{P_k}, P_j = [\gamma, \psi, B] \quad (25)$$

$$\text{PBR: } \eta = \omega_{St} \frac{St_c}{St} + \sum_{j=1}^3 \omega_{P_j} \frac{P_j}{P_k}, P_j = [\gamma, B, Da] \quad (26)$$

For the batch reactor, the critical values  $P_{j,c}$  are determined using the Adler–Enig (AE) criterion, whereas for the packed-bed reactor they are determined using the Henning–Perez (HP) criterion, consistent with the mechanistic formulations applied to each system. The  $\omega_{P_j}$  is the feature importance of  $P_j$  determined by the RF algorithm. By definition,  $\sum_{j=1}^3 \omega_{P_j} = 1$ , reflecting the relative contribution of each parameter to runaway onset. Predicting the extent of criticality is formulated as a regression task. Three algorithms were employed: Ridge Regression (RR), Random Forest (RF, 150 trees), and Support Vector Machine (SVM). The features were  $[\gamma, \psi, B, Da, St]$  and the output was  $\eta$ . Hyperparameters were tuned via random

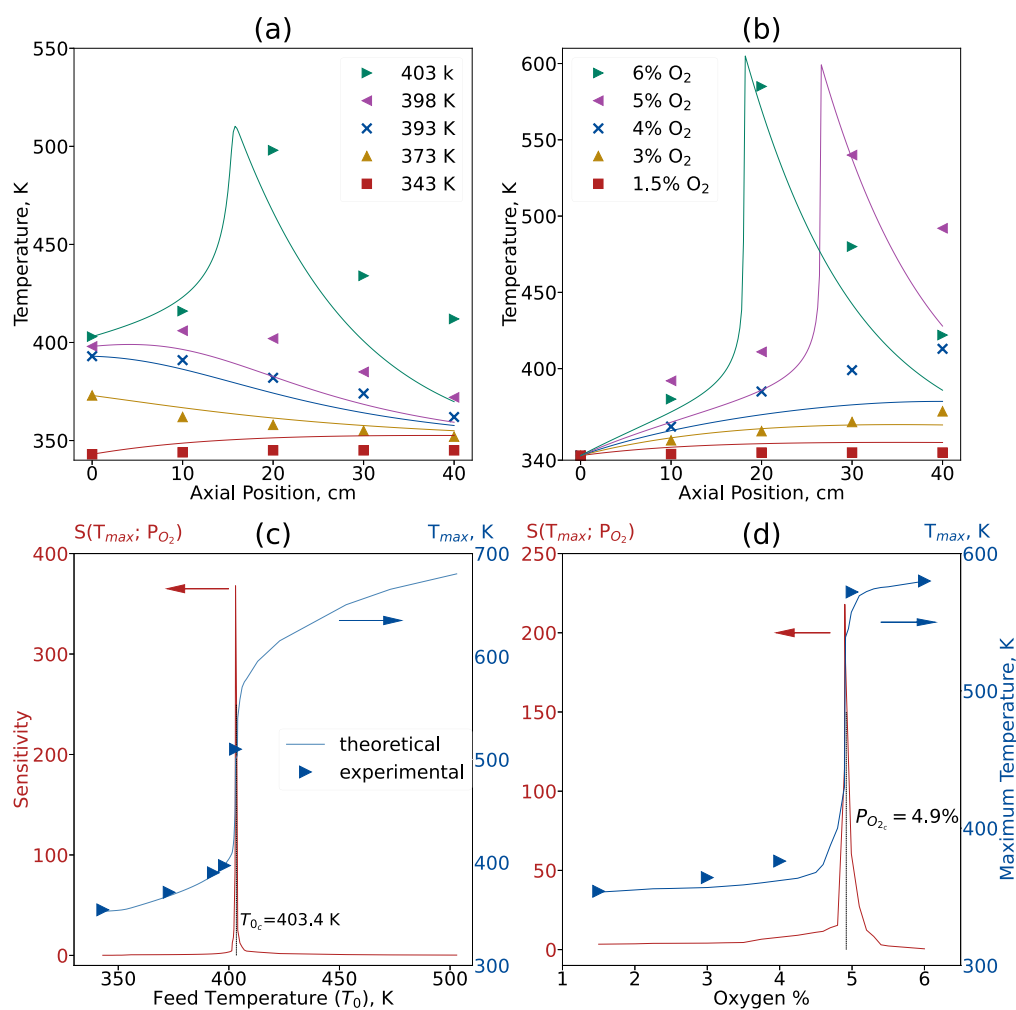


**Figure 2.** Comparison of experiments and model predictions with sensitivity analysis under differential fixed-bed operating conditions. All measurements were conducted at 343 K, 1 atm, using 0.02 g catalyst, a methanol feed rate of 0.6 mL/h (liquid, preheated to 343 K), and a total gas flow of 100 mL/min (6% CH<sub>3</sub>OH, 1.5% O<sub>2</sub>, 92.5% N<sub>2</sub>). Under these conditions, stable and near-critical cases exhibited <10% methanol conversion with ~95% selectivity to formaldehyde, whereas conditions close to thermal runaway exceeded 10% conversion and produced CO<sub>2</sub> as the dominant product. (a) Experimentally measured axial temperature profiles (points) compared with model predictions (curves) at varied feed temperatures, illustrating hotspot development. (b) Experimentally measured and model-predicted axial temperature profiles at varied oxygen concentrations. (c) Normalized sensitivity of maximum reactor temperature with respect to inlet temperature ( $T_0$ ), comparing model predictions and experiments. (d) Normalized sensitivity of maximum reactor temperature with respect to feed oxygen concentration, again comparing model and experiment. These operating conditions and measured conversion–selectivity trends provide the context for interpreting the hotspot behavior and the transition from selective oxidation to deep oxidation near the thermal runaway boundary.

search, consistent with the classification models (Tables S5–S8). Model performance was evaluated using the root-mean-square error (RMSE)

$$\text{RMSE} = \sqrt{\frac{\sum_{i=1}^n (y_i - f_i)^2}{n}} \quad (27)$$

where  $y_i$  are the observed values,  $f_i$  are the predicted values, and  $n$  is the number of observations.

### 3. RESULTS AND DISCUSSION

In our prior work,<sup>34</sup> extensive catalyst characterization was performed to elucidate the structure of Pt–Bi catalysts and to establish correlations between structure and catalytic activity. Characterization techniques included BET surface area analysis, H<sub>2</sub>-TPR (temperature-programmed reduction), ICP-AES (inductively coupled plasma–atomic emission spectroscopy), TEM (transmission electron microscopy), TEM-EDX

(energy-dispersive X-ray spectroscopy), TPO (temperature-programmed oxidation), XPS (X-ray photoelectron spectroscopy), and powder XRD (X-ray diffraction). From these measurements, we found that all Pt–Bi catalysts supported on activated carbon exhibited high surface areas (500–600 m<sup>2</sup>/g), pore sizes of 2.6–3.8 nm, and pore volumes of 0.7–1.5 cm<sup>3</sup>/g. Elemental analysis showed that the compositions of Pt and Bi in fresh catalysts were close to their designed loading values, whereas used catalysts exhibited 2–4 wt % losses of both metals, consistent with the unavoidable leaching reported previously.<sup>37,38</sup> XRD patterns of the bimetallic catalysts revealed no significant peaks between 5–90°, likely due to the small particle size (<3 nm), low metal loading (<5 wt %), and the strong background from the amorphous support.<sup>39,40</sup> TEM and H<sub>2</sub>–O<sub>2</sub> titration<sup>41</sup> gave consistent particle size estimates, while XPS and TEM-EDX confirmed strong electronic interactions between Pt and Bi species. Furthermore, H<sub>2</sub>-TPR analysis indicated a linear relationship between

catalyst reducibility and selectivity toward formaldehyde, and TPO demonstrated that the addition of Bi suppressed coke formation compared to the pure Pt catalyst.

### 3.1. Experimental Measurements and Mechanistic Model Validation

The criterion of Weisz and Prater,<sup>42</sup>  $\left(\frac{d_p^2 r_{p,cat}}{P_j D_{eff}} < 1\right)$ , was satisfied for all measurements, confirming the absence of mass transfer limitations in the kinetic data. External mass-transfer effects were also evaluated by performing flow-rate screening experiments at constant contact time ( $W/F$ ); the observed reaction rate remained unchanged for feed flow rates above 0.4 mL/h<sup>-1</sup>, demonstrating that gas–film resistance does not influence the measured kinetics. Sherwood numbers estimated from the Wakao–Funazkri correlation further confirmed that the external mass-transfer coefficient is large relative to the intrinsic reaction rate under all kinetic conditions, indicating that external diffusion limitations are negligible. A simple radial heat balance using Biot and Fourier numbers suggests that radial temperature differences in the packed bed are expected to be smaller than 2–4 K under stable conditions, but may grow to ca. 6 K near critical feed temperatures, consistent with the deviations observed. Because the fixed-bed reactor is a thin, elongated tube with  $L/D > 30$ , heat transfer is dominated by the axial direction and radial temperature gradients can be neglected under the operating conditions of this study. Together with the Weisz–Prater analysis confirming the absence of internal diffusion limitations, this indicates that the 1-D pseudohomogeneous model is reliable up to the onset of runaway, while deviations beyond that point arise from expected multidimensional heat and mass transfer effects. Because the one-dimensional pseudohomogeneous formulation is intended only to capture the low-conversion, prerunaway regime where intrinsic kinetics and minimal radial gradients remain valid, its role in this study is to identify the onset of instability rather than to reproduce multidimensional temperature fields during fully developed runaway. Because a one-dimensional pseudohomogeneous model cannot capture wrong-way behavior in packed-bed reactors, this is a fundamental limitation of the present mechanistic framework and future extensions incorporating heterogeneous two-energy-equation models, axial dispersion, and multidimensional heat-transfer descriptions will be required to resolve wrong-way dynamics and generate synthetic data sets that more fully represent such behavior for ML training. To gain mechanistic insight into the parametric sensitivity of Pt–Bi catalyst design and reactor operation for selective methanol oxidation, we first focus on the optimal 1%Pt–0.5%Bi catalyst, which achieved 8.1% methanol conversion, 98% selectivity, and 7.9% yield to formaldehyde under optimized conditions.<sup>34</sup> As established in our previous study on methanol oxidation, the experiments in Figure 2 were conducted under the same optimized differential-regime conditions; under these conditions, nonrunaway cases exhibit methanol conversion below 10%, whereas runaway cases exceed 10% conversion and CO<sub>2</sub> becomes the dominant product. Figure 1b shows the measured rate of the first reaction step as a function of methanol partial pressure. The rate displays a nearly linear dependence on  $P_{CH_3OH}$  and the slope provides the fitted value of the rate constant  $k_1$  under the specified operating conditions. Figure 1c presents Arrhenius plots for all five elementary reaction steps. The logarithm of each rate constant decreases linearly with 1/

$T$ , allowing extraction of apparent activation energies and illustrating the relative temperature sensitivities of the individual reaction pathways. Because methanol conversion values were consistently below  $\sim 10\%$ , differential kinetics applied, as described by Eq. 28. Although strongly exothermic reactions may give rise to radial temperature gradients in cooled packed-bed reactors, a quantitative assessment based on dimensionless analysis and a simplified two-dimensional energy balance indicates that such gradients remain secondary under the operating conditions considered. Accordingly, a one-dimensional axial model is retained to capture hotspot development and proximity to thermal runaway, while details of the radial-gradient assessment are provided in the Supporting Information.

$$r_i = \frac{F_{(i+2)}}{\alpha_{(i+2)}W} \quad (28)$$

Using this framework, reaction orders of CH<sub>3</sub>OH ( $n_{(1,1)}$ ) and O<sub>2</sub> ( $n_{(1,2)}$ ) in step R<sub>1</sub> were determined. Figure 1b shows that assuming  $n_{(1,1)} = n_{(1,2)} = 1$  yields linear fits of  $r_1/P_{O_2}^{n_{(1,2)}}$  versus  $P_{CH_3OH}$  and  $r_1/P_{CH_3OH}^{n_{(1,1)}}$  versus  $P_{O_2}$ , providing consistent values of  $k_1$ . Alternative assumptions with higher orders (e.g.,  $n_{(1,1)} = 1, n_{(1,2)} = 2$ ;  $n_{(1,1)} = n_{(1,2)} = 2$ ) resulted in poorer fits, supporting the validity of first-order kinetics for both CH<sub>3</sub>OH and O<sub>2</sub> in R<sub>1</sub>. Similar analyses for steps R<sub>2</sub>–R<sub>5</sub> showed that first-order dependencies consistently provided the best fits, likely owing to the low conversion and partial pressures (<0.1 atm) of both CH<sub>3</sub>OH and O<sub>2</sub>. The Arrhenius plots for all five steps (Figure 1c) showed excellent linearity, from which activation energies ( $E_{a,i}$ ) and pre-exponential factors ( $A_i$ ) were extracted (Table S2). Because the Pt–Bi/activated-carbon catalyst studied here is a novel low-temperature selective-oxidation system, the activation energies and rate constants extracted in this work represent, to the best of our knowledge, the first experimentally determined kinetic parameters reported for this catalyst, thereby providing a necessary basis for the mechanistic modeling framework developed in this study. Additional supporting results, including dew point temperature calculations (Table S3) and kinetic parameters for the 1%Pt and 1%Pt–0.2%Bi catalysts (Table S4), are also provided. A 95% confidence intervals for the activation energies and pre-exponential factors is obtained in Table S2. Among the five steps, R<sub>1</sub> (formaldehyde formation) and R<sub>5</sub> (CO<sub>2</sub> formation) dominated, with R<sub>5</sub> displaying the strongest temperature dependence due to its higher activation energy (76.9 kJ/mol vs 15.6 kJ/mol for R<sub>1</sub>). At the reactor scale, the kinetic model was validated against experimental axial temperature profiles. Figure 2a compares experimental and model-predicted results at different feed temperatures ( $T_0 = 343$ –403 K). Good agreement was obtained at moderate feed temperatures (343–393 K), where both experiment and model showed relatively steady profiles. At higher  $T_0$  values, however, hot spots appeared: at 398 K a minor local maximum emerged, while at 403 K both experiment and model captured a sharp runaway, with peak reactor temperatures near 500 K. Under nonrunaway conditions the mechanistic model reproduces the measured axial temperature profiles, while under runaway-prone conditions the model correctly identifies the onset of thermal runaway even though the full runaway trajectory cannot be experimentally accessed. Figure 2b shows similar trends for varied feed oxygen concentrations (1.5–6% O<sub>2</sub> at constant 6% CH<sub>3</sub>OH). Stable operation was observed at 1.5–4% O<sub>2</sub>,

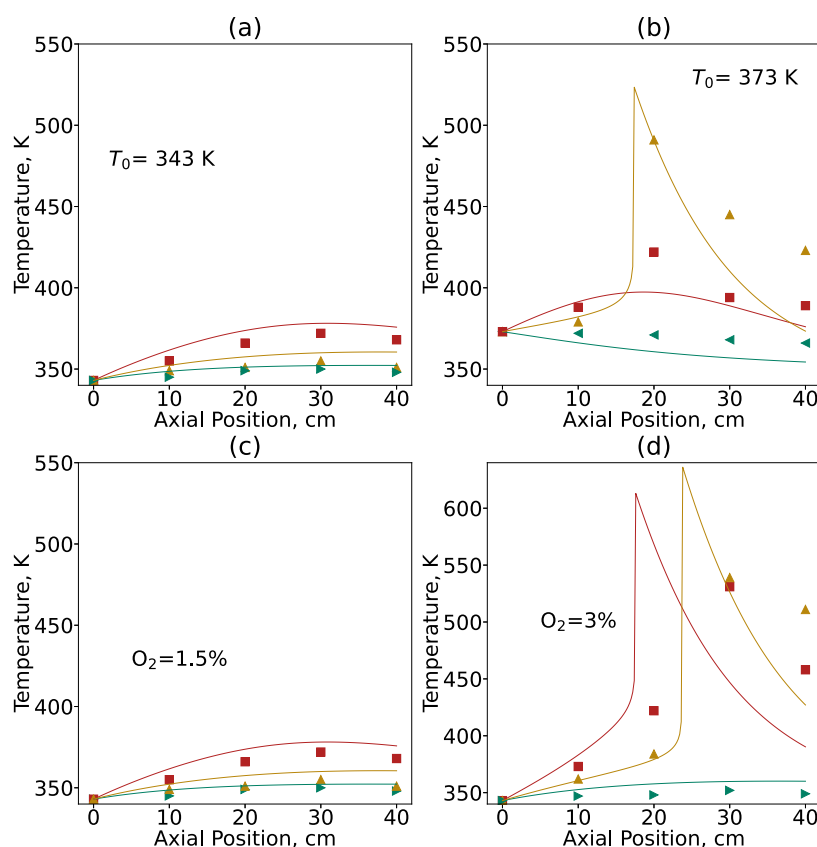


**Figure 3.** Sensitivity of Pt–Bi bimetallic catalyst design on reactor thermal performance: (a) Axial temperature profiles at  $T_0 = 343$  K for 1%Pt, 1% Pt–0.2%Bi, and 1%Pt–0.5%Bi catalysts. (b) Axial temperature profiles at  $T_0 = 373$  K for the same catalysts, showing more pronounced hot-spot formation for 1%Pt and 1%Pt–0.2%Bi. (c) Axial temperature profiles at 1.5%  $O_2$  feed, where all three catalysts remain thermally stable. (d) Axial temperature profiles at 3%  $O_2$  feed, where both 1%Pt and 1%Pt–0.2%Bi exhibit runaway behavior while 1%Pt–0.5%Bi maintains relatively stable performance.

whereas hot spots developed at 5–6%  $O_2$ , marking the onset of runaway. In these extreme cases, model predictions deviated somewhat from experiments, likely due to effects not captured by the one-dimensional pseudohomogeneous model, such as external mass transfer resistance, radial thermal gradients, and extrapolation beyond the valid kinetic range. Nonetheless, the simple reactor model successfully predicted the onset of thermal runaway with reasonable accuracy. Although the predicted and measured axial temperature profiles do not match perfectly at the highest feed oxygen concentrations (Figure 2b), this deviation arises primarily because methanol conversion increases substantially as the system approaches the critical boundary, whereas the kinetic parameters were determined under strictly differential conditions with conversion below 10%. The pseudohomogeneous model therefore remains essentially valid in the prerunaway regime for which it was designed, where both temperature gradients and conversions remain small and intrinsic kinetics are directly applicable. Even with these expected deviations near the critical point, the model accurately identifies the onset of thermal runaway, as evidenced by the close agreement between the experimentally observed and model-predicted critical inlet temperature and oxygen concentration. This confirms that the pseudohomogeneous formulation is sufficiently reliable for mapping the runaway boundary, which is the central objective of the mechanistic component of this study.

Normal hotspot formation in selective methanol oxidation produces bounded, convex axial temperature profiles asso-

ciated with controlled conversion increases, whereas conditions near the instability boundary display a rapid transition toward concave, accelerating temperature behavior; because only this onset regime is experimentally accessible under safety constraints, the sensitivity-based AE and HP criteria provide an appropriate and practical means of identifying the loss of stability. The predictive capability of the model was further assessed using sensitivity analysis of  $T_{max}$  with respect to feed temperature ( $T_0$ ) and oxygen concentration ( $P_{O_2}$ ). Figure 2c shows that  $S(T_{max}; T_0)$  remained close to zero for  $T_0 < 403$  K, but rose sharply when  $T_0$  reached its critical value (403.4 K), coinciding with the experimentally observed runaway threshold (403 K). A similar result was obtained for oxygen concentration (Figure 2d), where sensitivity increased abruptly at a critical  $P_{O_2}$  of 4.9%, in close agreement with the experimental observation of 5%. Across all operating conditions in Figure 2a and 2b, the mean absolute deviation between the measured and modeled temperatures is 2–4 K, with maximum deviations below 6 K near the critical boundary, demonstrating that the model describes the axial thermal behavior with good accuracy up to the onset of runaway. These results demonstrate that the combination of detailed kinetic modeling and sensitivity analysis not only reproduces stable reactor performance, but also accurately identifies the critical conditions for the onset of thermal runaway. We note that discrepancies between model predictions and experimental temperature profiles may partly

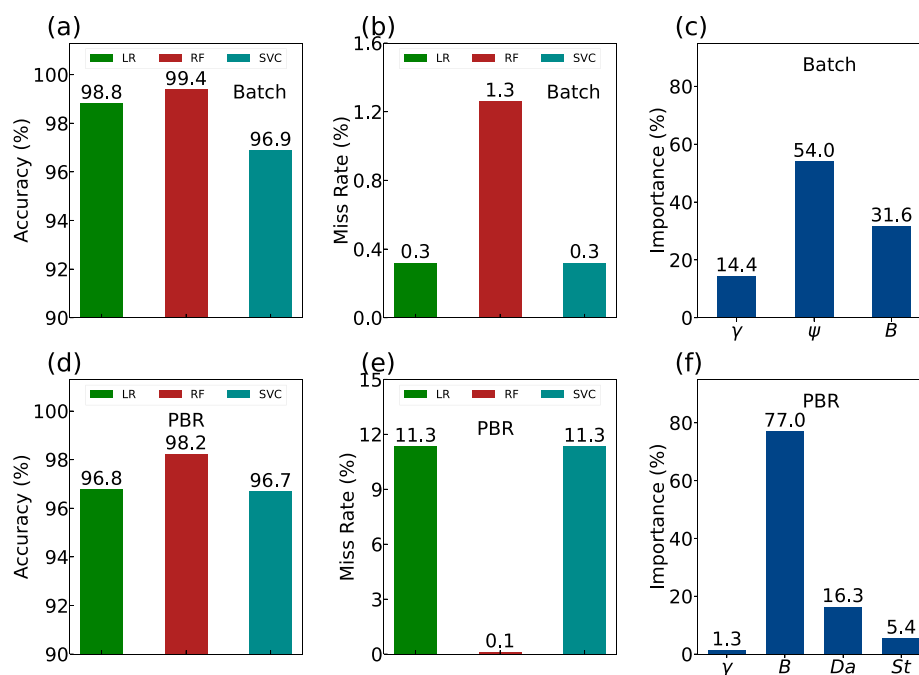


**Figure 4.** Classification results for predicting thermal runaway onset using Logistic Regression (LR), Random Forest (RF), and Support Vector Classification (SVC). (a) Mean accuracies for the acetic anhydride hydrolysis batch reactor: LR (98.81%), RF (99.37%), SVC (96.88%). (b) Mean miss rates for the batch reactor: LR (0.32%), RF (1.26%), SVC (0.32%). (c) Relative importance of dimensionless parameters ( $\gamma$ ,  $\psi$ ,  $B$ ) derived from the Random Forest algorithm for the batch reactor. (d) Mean accuracies for the methanol oxidation packed-bed reactor (PBR): LR (96.77%), RF (98.23%), SVC (96.68%). (e) Mean miss rates for the PBR: LR (11.33%), RF (0.1053%), SVC (11.33%). (f) Relative importance of dimensionless parameters ( $\gamma$ ,  $B$ ,  $Da$ ,  $St$ ) derived from the Random Forest algorithm for the PBR.

arise from uncertainties in the effective heat-transfer description. Because detailed heat-transfer coefficients and temperature-dependent transport properties were not independently measured in this study, the model is intended to capture trends and runaway proximity rather than exact local temperature magnitudes.

### 3.2. Mechanistic Sensitivity and Parametric Analysis of Catalyst Design

In addition to feed conditions, catalyst composition strongly influences reactor thermal stability. To investigate this effect, three representative catalysts—1%Pt, 1%Pt–0.2%Bi, and the optimal 1%Pt–0.5%Bi—were evaluated. The kinetic parameters for these catalysts (Table S2) revealed distinct behaviors. For the 1%Pt catalyst, step  $R_5$  ( $\text{CO}_2$  formation) dominated due to its relatively low activation energy (26.7 kJ/mol), whereas all other steps exhibited much higher barriers (142–186 kJ/mol). For the 1%Pt–0.2%Bi catalyst, both  $R_1$  (formaldehyde formation) and  $R_5$  were favored at lower temperatures, while the other three steps became relevant only at higher temperatures. In contrast, the balanced Pt–Bi composition in the 1%Pt–0.5%Bi catalyst promoted steady thermal performance by distributing activity more evenly across reaction pathways. Figure 3a–b compares axial temperature profiles at feed temperatures of 343 and 373 K. At 343 K, all three catalysts showed relatively steady behavior, though a minor hot spot appeared for the 1%Pt catalyst due to strong  $\text{CO}_2$  formation. At 373 K, the difference between catalysts became more evident: the 1%Pt–0.2%Bi catalyst exhibited incipient runaway, the 1%Pt catalyst showed a more pronounced hot spot, while the 1%Pt–0.5%Bi catalyst remained stable. When feed temperature increased further (not shown in Figure 3), both 1%Pt and 1%Pt–0.2%Bi catalysts underwent runaway at

393 K, whereas the 1%Pt–0.5%Bi catalyst maintained steady performance until 403 K, beyond which runaway was unavoidable for all compositions. A similar trend was observed for oxygen concentration (Figure 3c–d). At 1.5%  $\text{O}_2$ , all three catalysts operated steadily without hot-spot formation. At 3%  $\text{O}_2$ , however, the 1%Pt and 1%Pt–0.2%Bi catalysts exhibited rapid runaway with reactor temperatures exceeding 550 K, while the 1%Pt–0.5%Bi catalyst showed a delayed and less severe thermal response. These results highlight that the addition of Bi suppresses the highly exothermic  $\text{CO}_2$  pathway, thereby reducing thermal instability and extending the safe operating window. In summary, Figure 3 demonstrates that careful tuning of Bi promoter content is essential. While excessive Bi lowers catalytic activity, moderate Bi loading (0.5%) provides a balance between high formaldehyde selectivity and stable thermal performance, thereby minimizing the risk of thermal runaway under both temperature and oxygen perturbations. These catalyst-comparison results establish that the mechanistic trends embedded in the reaction network—and therefore in the synthetic ML data sets—are experimentally consistent across several Pt–Bi compositions.

### 3.3. Machine-Learning Classification of Runaway Onset

The generated data sets include 53.48% runaway cases for the batch reactor and 31.33% for the packed-bed reactor. The generated data sets were constructed to match the proportions observed in the experimental test sets (50% for the batch reactor, 28% for the PBR) through stratified sampling. This ensured that the ML models learned from realistic class distributions, avoiding artificial balancing biases and improving generalizability. Predicting the onset of thermal runaway was formulated as a classification problem. Three algorithms were applied: Logistic Regression (LR), Random Forest (RF), and

Support Vector Classification (SVC). The features consisted of the dimensionless parameter set  $[\gamma, \psi, B, Da, St]$ , and the output variable was  $R$ . Hyperparameters were tuned by random search, while Figure 4(a, c) shows the mean accuracies for the batch reactor and the PBR, respectively, while Figure 4(b, d) shows the corresponding miss rates. Performance of training and 3-fold cross-validation is summarized in Tables S9–S10. For the acetic anhydride batch reactor, all three algorithms achieved near-perfect test accuracy (LR: 98.81%, RF: 99.37%, SVC: 96.88%). For the methanol oxidation PBR, accuracy was slightly lower but remained above 95% (LR: 96.77%, RF: 98.23%, SVC: 96.68%). Since accuracy alone does not capture the safety implications of misclassification, the miss rate (false negative rate) was used as a critical metric. From a process safety perspective, false positives (predicting runaway when safe) are acceptable, but false negatives (predicting safe when runaway) can be catastrophic. RF consistently achieved the lowest miss rates for PBR (0.1053%), compared to LR and SVC (11.33%), while maintaining comparable low miss rates for Batch (RF = 1.26%, LR = 0.32%, and SVC = 0.32%). The consistently high accuracy and low miss rate for the batch reactor are attributed to its mechanistic simplicity, involving only a single reaction pathway. In contrast, the methanol oxidation PBR is more complex, with five parallel reactions and normalization parameters, which increases variance and reduces predictive accuracy. Overall, the Random Forest algorithm emerged as the most reliable classification model for predicting the onset of thermal runaway in both the batch and fixed-bed systems studied here. In addition to classification performance, Random Forest analysis provided insights into the relative importance of input parameters (Figure 4e–f). For the batch reactor, the Semenov number  $\psi$  is the most influential feature, followed by the dimensionless heat of reaction  $B$  and the activation-energy parameter  $\gamma$ . For the packed-bed reactor, the dimensionless heat of reaction  $B$  dominates the feature importance, with  $Da$  and  $St$  contributing to a lesser extent and  $\gamma$  having minimal influence. In this packed-bed system, the dominance of the dimensionless heat of reaction  $B$  arises because runaway behavior is driven mainly by the magnitude of heat release associated with deep oxidation pathways, whereas the external heat-transfer resistance is not rate-limiting under the operating conditions considered; as a result,  $B$  outweighs  $Da$  and  $St$  in determining the proximity to runaway. These results demonstrate that the ML framework not only predicts runaway onset with high reliability, but also yields interpretable parameter importance consistent with mechanistic understanding. Once the ML models are trained, they can be deployed in industrial reactor systems as a real-time safety and decision-support tool. By continuously evaluating the relevant dimensionless inputs and updating the ML-informed criticality metric  $\eta$ , operators can rapidly determine whether current operating conditions fall within a safe region, a high-risk transitional zone, or are approaching the onset of runaway. Such rapid assessment is particularly important in time-sensitive scenarios, where unexpected temperature excursions may require immediate intervention and where classical mechanistic calculations may be too slow for operational use. The proposed framework therefore has the potential to complement existing monitoring and control systems and to enhance thermal-safety management at industrial scale. Because the feature-importance patterns arise primarily from the numerical ranges of the sampled dimensionless parameters, the weighting factors are

transferable to other strongly exothermic reaction systems whose dimensionless groups fall within similar ranges; only the kinetic normalization used in constructing the  $\psi$  term is reaction-specific and must be recalculated once for a new chemistry.

### 3.4. Machine-Learning Prediction of Runaway Intensity

While classification models predict whether a reactor will undergo runaway, they cannot quantify how close a system is to instability. To address this gap, we propose a machine-learning-based criterion,  $\eta$ , which measures the extent of criticality and thereby quantifies thermal runaway intensity. Building on the equal-weighted definition of  $\eta'$  from Section 2.4, the ML-based criterion  $\eta$  incorporates feature importance values  $\omega_j$  derived from the Random Forest algorithm:

$$\eta = \sum_j \omega_j \frac{P_j}{P_k}, \quad \sum_j \omega_j = 1 \quad (29)$$

Here,  $P_j$  are the dimensionless parameters ( $\gamma, \psi, B$  for batch reactors;  $\gamma, B, Da, St$  for PBRs), and  $P_k$  are their corresponding critical values calculated from classical criteria. By construction,  $\eta = 1$  at the runaway boundary,  $\eta < 1$  for stable operation, and  $\eta > 1$  for runaway conditions. The feature weights  $\omega_j$  ensure that dominant parameters, such as  $St$  and  $Da$  in PBRs or  $\gamma$  and  $B$  in batch reactors (Figure 4e–f), contribute proportionally to the criticality measure. Unlike classical single-reaction stability criteria such as the Semenov parameters, which assume that thermal runaway is driven by a single dominant exothermic pathway, the metric  $\eta$  incorporates reaction-weighting factors that reflect the contributions of all five parallel oxidation routes in the mechanistic model. As a result,  $\eta$  captures pathway switching and multipathway coupling near the runaway boundary, effects that classical criteria do not represent. Once trained,  $\eta$  provides a continuous and directly computable indicator of proximity to runaway using only the dimensionless inputs, and the associated feature-importance values offer a transparent interpretation of which dimensionless groups exert the strongest influence on instability. The regression performance of the ML-based  $\eta$  was benchmarked against values from mechanistic models. Figure 5 shows that the RF regression model predicts  $\eta$  with excellent agreement, capturing both safe and runaway regions as well as the transitions between them. This confirms that  $\eta$  provides a robust and interpretable measure of thermal runaway intensity. Beyond prediction,  $\eta$  offers several practical applications. First, it enables recognition of reactors that are highly risky but not yet explosive. For example, a system with  $\eta = 0.99$  would be labeled “safe” by a classification model, yet its proximity to the boundary indicates a high likelihood of runaway under small perturbations. Second,  $\eta$  introduces an economic dimension to reactor operation. Extremely low  $\eta$  values (e.g., 0.05) guarantee safety but incur high cooling costs, while moderate  $\eta$  values (e.g., 0.2) balance safety and efficiency. Finally,  $\eta$  can serve as a real-time monitoring signal: when  $\eta$  approaches 0.9, the control system can trigger alarms and corrective actions before reaching runaway conditions. Because  $\eta$  is defined as a continuous measure of proximity to the mechanistic runaway boundary, we classified operating conditions by mapping  $\eta$  onto a graded risk scale. Specifically,  $\eta = 1$  corresponds exactly to the onset of runaway determined by the AE or HP criterion, values of  $\eta > 1$  denote supercritical (runaway) conditions, and values of  $\eta < 1$  represent subcritical operation. Intermediate thresholds were

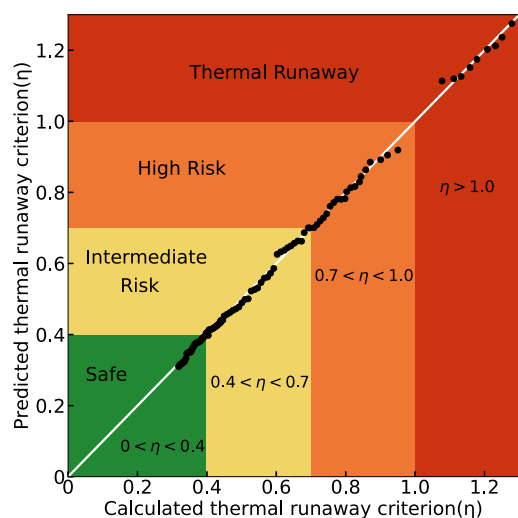


**Figure 5.** Prediction of thermal runaway intensity using the machine-learning-based criterion  $\eta$ . Scatter plot of  $\eta$  values calculated from classical mathematical models versus those predicted by the Random Forest (RF) regression model. Risk levels are visibly divided into four regions:  $0 < \eta < 0.4$  (safe),  $0.4 < \eta < 0.7$  (intermediately risky),  $0.7 < \eta < 1.0$  (highly risky), and  $\eta > 1.0$  (thermal runaway). The close alignment of predicted and calculated values demonstrates the ability of the RF algorithm to capture the extent of criticality with high fidelity.

selected based on the temperature distance from the mechanistic runaway point (within approximately 2 K for the high-risk region) to provide a practical, interpretable risk classification for operators. These thresholds are adjustable and serve as an initial mapping of the continuous  $\eta$  metric to discrete risk categories. Note that machine learning in this work is not intended to replace mechanistic modeling; rather, it accelerates prediction once a validated kinetics–transport framework is established. ML classifiers inherit the underlying physics through AE- and HP-derived labels and therefore serve only as complementary tools for rapid screening near the runaway boundary. In this framework, the classical runaway criteria are used only once—during data set generation—to compute the critical values  $P_{j,c}$  that define the onset boundary. After training, the ML model predicts  $\eta$  directly from the dimensionless inputs without further numerical solution of the reactor balances; mechanistic modeling is needed only to create the initial labeled data set for a new reaction system. In summary, the proposed criterion  $\eta$  extends ML-based classification models by providing a continuous, interpretable measure of thermal runaway intensity. It bridges the gap between mechanistic thresholds and operational decision-making, offering both predictive accuracy and practical utility for industrial reactor safety.

#### 4. CONCLUDING REMARKS

Thermal runaway remains one of the most critical challenges in chemical process safety, as uncontrolled temperature escalation can lead to catastrophic reactor failure, human casualties, and economic loss. While numerous mechanistic criteria have been developed to predict runaway onset, they often require solving complex systems of equations and are restricted to single-reaction mechanisms. This creates a knowledge gap in developing practical tools that can link experimental data, kinetic modeling, and modern machine learning approaches

into a unified framework for predicting both the onset and intensity of thermal runaway. In this work, we addressed this gap through a combined experimental, modeling, and data-driven approach. Mechanistic kinetic analysis of methanol oxidation over Pt–Bi catalysts validated the reactor model and identified key reaction steps, with  $R_1$  (formaldehyde formation) and  $R_3$  ( $\text{CO}_2$  formation) dominating temperature sensitivity. Reactor-scale simulations showed that feed temperature and oxygen concentration strongly control thermal stability, with the simple pseudohomogeneous model successfully predicting the onset of runaway. The influence of catalyst design was also examined, demonstrating that moderate Bi promotion (0.5% Bi) balances activity and selectivity while suppressing runaway, whereas excessive or insufficient Bi loading destabilizes reactor performance. Machine learning was then employed to complement mechanistic models. Classification algorithms were trained to predict runaway onset ( $R = 0/1$ ) using dimensionless reactor parameters. All models achieved high accuracy, with Random Forest (RF) delivering the lowest miss rates, a critical factor for avoiding false negatives that could misclassify runaway as safe operation. We further proposed a new ML-based criterion,  $\eta$ , to quantify the intensity of thermal runaway. RF regression predicted  $\eta$  with high fidelity against mechanistic models, and  $\eta$  divided reactor states into safe, intermediate, highly risky, and runaway regions, providing a continuous and interpretable measure of criticality. These results establish a pragmatic framework that unifies mechanistic insight with machine learning prediction. Beyond advancing predictive capabilities, the ML-based criterion  $\eta$  introduces a practical dimension to reactor safety management: balancing safety margins, economic cost, and real-time monitoring. Looking forward, this framework can be extended to more complex systems, including multiscale reactor networks, additional catalyst architectures, and dynamic operational disturbances. Such integration holds promise for developing adaptive digital twins for chemical reactors, demonstrated here on batch and fixed-bed reactors, and formulated to be capable of forecasting and preventing thermal runaway in industrial practice.

#### ■ ASSOCIATED CONTENT

##### Supporting Information

The Supporting Information is available free of charge at <https://pubs.acs.org/doi/10.1021/acs.iecr.5c04085>.

Definitions of dimensionless groups used in the thermal runaway analysis; assessment of radial temperature gradients and model dimensionality; detailed kinetic and thermodynamic parameters; dew-point calculations; numerical procedures for generating synthetic data sets; descriptions of machine-learning model construction and hyperparameter tuning; tables of model performance metrics; and a numerical example illustrating the calculation of the criticality metric  $\eta$  for a packed-bed reactor (PDF)

#### ■ AUTHOR INFORMATION

##### Corresponding Author

Yang Xiao – Institute for Micromanufacturing and Department of Chemical Engineering, Louisiana Tech University, Ruston, Louisiana 71272, United States; [orcid.org/0000-0003-1705-2213](https://orcid.org/0000-0003-1705-2213); Phone: 318-257-5109; Email: [yxiao@latech.edu](mailto:yxiao@latech.edu); Fax: 318-257-4000

## Authors

Tobias K. Misicko – Institute for Micromanufacturing and Department of Chemical Engineering, Louisiana Tech University, Ruston, Louisiana 71272, United States

Joaquin Herrero – Institute for Micromanufacturing and Department of Chemical Engineering, Louisiana Tech University, Ruston, Louisiana 71272, United States

Jacob C. Robinson – Institute for Micromanufacturing and Department of Chemical Engineering, Louisiana Tech University, Ruston, Louisiana 71272, United States

Daniela S. Mainardi – Institute for Micromanufacturing and Department of Chemical Engineering, Louisiana Tech University, Ruston, Louisiana 71272, United States

Complete contact information is available at: <https://pubs.acs.org/10.1021/acs.iecr.5c04085>

## Author Contributions

<sup>†</sup>T.K.M., J.H., and J.C.R. contributed equally.

## Notes

The authors declare no competing financial interest.

## ACKNOWLEDGMENTS

We are delighted to contribute to the Special Issue of *Industrial & Engineering Chemistry Research*, 2025 NASCRE-5: Breaking Barriers for a Sustainable Future. We would like to acknowledge with deep respect the late Prof. Arvind Varma of Purdue University, the Ph.D. advisor and postdoctoral supervisor of Y.X., who unfortunately passed away in 2019. Prof. Varma's pioneering contributions to the study of thermal runaway in chemical reactors, together with his encouragement for Y.X. to explore this research area, continue to inspire our work. His impact on the field, and on our research journey, will be remembered with gratitude. The authors also gratefully acknowledge Dr. Kaida Liu for his early-stage discussions and initial technical insights that helped shape this study. This work was supported by start-up funds from the College of Engineering and Science at Louisiana Tech University. This material is also based, in part, upon work supported by the U.S. Department of Energy, Office of Science, Office of Workforce Development for Teachers and Scientists, under the Office of Science Graduate Student Research (SCGSR) program. The SCGSR program is administered by the Oak Ridge Institute for Science and Education (ORISE) for the DOE under contract number DE-SC0014664.

## NOMENCLATURE

|                   |  |
|-------------------|--|
| $A_b$             | $m^2$ Heat exchange surface area on the bed side   |
| $A_i$             | $kmol \cdot kg_{cat}^{-1} \cdot s^{-1} \cdot atm^{-n_{(i,1)}-n_{(i,2)}}$ Pre-exponential factor of step $i$ when the reaction order is $n_i$ |
| $A_m$             | $m^2$ Log-mean of $A_b$ and $A_u$  |
| $A_u$             | $m^2$ Heat exchange surface area on the heat-transfer medium side  |
| B                 | - Dimensionless heat of reaction   |
| $B_n$             | - Contribution of reaction step $n$ to B   |
| $C_{1j} - C_{5j}$ | $kJ \cdot kmol^{-1} \cdot K^{-1}$ DIPPR parameters   |
| $C_{6j} - C_{7j}$ | $K$ DIPPR parameters   |
| $C_i$             | $kmol \cdot m^{-3}$ Inlet concentration of limiting reactant   |
| $c_p$             | $kJ \cdot kmol^{-1} \cdot K^{-1}$ Heat capacity of mixture   |
| $c_{p_j}$         | $kJ \cdot kmol^{-1} \cdot K^{-1}$ Heat capacity of species $j$   |
| $D_a$             | - Dimensionless geometric parameter  |
| $D_{eff}$         | $m^2 \cdot s^{-1}$ Effective diffusion coefficient   |

|                              |   |
|------------------------------|---|
| $D_i$                        | $m$ Reactor inner diameter  |
| $D_o$                        | $m$ Reactor outer diameter  |
| $d$                          | $m$ Thickness of reactor wall   |
| $d_p$                        | $m$ Catalyst particle diameter  |
| $\bar{d}_i$                  | $m$ Internal reactor diameter   |
| Da                           | - Damköhler Number  |
| $E_a$                        | $kJ \cdot kmol^{-1}$ Activation energy (scalar)   |
| $E_{a_i}$                    | $kJ \cdot kmol^{-1}$ Activation energy of step $R_i$  |
| $F$                          | $kmol \cdot s^{-1}$ Total flow rate   |
| $F_0$                        | $kmol \cdot s^{-1}$ Feed flow rate  |
| $F_j$                        | $kmol \cdot s^{-1}$ Flow rate of species $j$  |
| $k_i$                        | $kmol \cdot kg_{cat}^{-1} \cdot s^{-1} \cdot atm^{-n_{(i,1)}-n_{(i,2)}}$ Reaction rate constant of step $i$ |
| $k_n$                        | $kmol \cdot kg_{cat}^{-1} \cdot s^{-1}$ Rate constant of reaction step $n$                                  |
| $n_{(ij)}$                   | - Reaction order for species $j$ in $R_i$   |
| Nu <sub><math>i</math></sub> | - Nusselt number for bed-side heat transfer   |
| $P_0$                        | $atm$ Feed pressure   |
| $P_i$                        | $atm$ Inlet partial pressure of limiting reactant   |
| $P_j$                        | $atm$ Partial pressure of species $j$   |
| $P_{j,c}$                    | - Critical value of dimensionless group $P_j$   |
| $P_{total}$                  | $atm$ Total pressure  |
| Pr                           | - Prandtl number of gas mixture   |
| $\phi$                       | - Generic model parameter in sensitivity analyses   |
| $r_1$                        | $kmol \cdot kg_{cat}^{-1} \cdot s^{-1}$ Reaction rate of step $R_1$   |
| $r_i$                        | $kmol \cdot kg_{cat}^{-1} \cdot s^{-1}$ Reaction rate of step $R_i$   |
| Re                           | - Reynolds number based on $D_i$  |
| R                            | - runaway indicator   |
| $R_g$                        | $kJ \cdot kmol^{-1} \cdot K^{-1}$ Gas constant = 8.314  |
| $s(T_{max}; \phi)$           | - Sensitivity of $T_{max}$ with respect to $\phi$   |
| $S(T_{max}; \phi)$           | - Normalized sensitivity of $T_{max}$ wrt $\phi$  |
| $S_v$                        | $m^{-1}$ Heat-transfer area per reactor volume  |
| St                           | - Stanton Number  |
| $St_c$                       | - Critical Stanton number   |
| $St_n$                       | - Contribution of step $n$ to St  |
| $T$                          | $K$ Reaction temperature  |
| $T_0$                        | $K$ Feed temperature  |
| $T_c$                        | $K$ Coolant temperature   |
| $T_i$                        | $K$ Reference temperature for nondimensionalization   |
| $T_{max}$                    | $K$ Maximum temperature   |
| $U$                          | $kJ \cdot m^{-2} \cdot K^{-1} \cdot s^{-1}$ Overall heat transfer coefficient                               |
| $W$                          | $kg$ Amount of packed catalyst  |

## Greek Letters:

|                  |   |
|------------------|---|
| $\alpha_i$       | $kJ \cdot m^{-2} \cdot K^{-1} \cdot s^{-1}$ Bed-side heat transfer coefficient    |
| $\alpha_u$       | $kJ \cdot m^{-2} \cdot K^{-1} \cdot s^{-1}$ Medium-side heat transfer coefficient |
| $\alpha_{(ij)}$  | - Stoichiometric coefficient for species $j$ in $R_i$                             |
| $\Delta H_{r_i}$ | $kJ \cdot kmol^{-1}$ Enthalpy change of reaction $i$                              |
| $\eta$           | - ML-based criticality metric   |
| $\gamma$         | - Dimensionless activation energy   |
| $\lambda$        | $kJ \cdot m^{-1} \cdot K^{-1} \cdot s^{-1}$ Thermal conductivity of reactor wall  |
| $\lambda_g$      | $W \cdot m^{-1} \cdot K^{-1}$ Thermal conductivity of reactant gas mixture        |
| $\lambda_{air}$  | $W \cdot m^{-1} \cdot K^{-1}$ Thermal conductivity of air                         |
| $\psi$           | - Heat-generation sensitivity parameter   |
| $\Psi$           | - Semenov number  |
| $\rho_{cat}$     | $kg \cdot m^{-3}$ Packed catalyst density   |
| $\sigma_n$       | - Kinetic weighting factor of step $n$  |
| $\theta$         | - Dimensionless temperature   |
| $\theta_a$       | - Dimensionless ambient temperature   |
| $\theta_{co}$    | - Dimensionless coolant temperature   |
| $\omega_B$       | - Feature-importance weight for B   |
| $\omega_{Da}$    | - Feature-importance weight for Da  |

- $\omega_\gamma$  - Feature-importance weight for  $\gamma$   
 $\omega_j$  - ML feature-importance weight  
 $\omega_{P_j}$  - Weight of parameter  $P_j$  in definition of  $\eta$   
 $\omega_{St}$  - Weight associated with  $\frac{St_c}{St}$  term

## REFERENCES

- (1) Balasubramanian, S. G.; Louvar, J. F. Study of Major Accidents and Lessons Learned. *Process Safety Progress* **2002**, *21* (3), 237–244.
- (2) Dakkoune, A.; Vernieres-Hassimi, L.; Leveneux, S.; Lefebvre, D.; Estel, L. Risk Analysis of French Chemical Industry. *Safety Science* **2018**, *105*, 77–85.
- (3) Semenov, N. Zur Theorie des Verbrennungsprozesses. *Z. Physik* **1928**, *48*, 571–582.
- (4) Thomas, P. H.; Bowes, P. C. Some Aspects of the Self-Heating and Ignition of Solid Cellulosic Materials. *British Journal of Applied Physics* **1961**, *12* (5), 222–229.
- (5) Adler, J.; Enig, J. The Critical Conditions in Thermal Explosion Theory with Reactant Consumption. *Combust. Flame* **1964**, *8* (2), 97–103.
- (6) Morbidelli, M.; Varma, A. Parametric Sensitivity and Runaway in Tubular Reactors. *AIChE J.* **1982**, *28* (5), 705–713.
- (7) Morbidelli, M.; Varma, A. On Parametric Sensitivity and Runaway Criteria of Pseudohomogeneous Tubular Reactors. *Chem. Eng. Sci.* **1985**, *40* (11), 2165–2168.
- (8) Morbidelli, M.; Varma, A. A Generalized Criterion for Parametric Sensitivity: Application to Thermal Explosion Theory. *Chem. Eng. Sci.* **1988**, *43* (1), 91–102.
- (9) Morbidelli, M.; Varma, A. A Generalized Criterion for Parametric Sensitivity: Application to a Pseudohomogeneous Tubular Reactor with Consecutive or Parallel Reactions. *Chem. Eng. Sci.* **1989**, *44* (8), 1675–1696.
- (10) Wu, H.; Morbidelli, M.; Varma, A. An Approximate Criterion for Reactor Thermal Runaway. *Chem. Eng. Sci.* **1998**, *53* (18), 3341–3344.
- (11) Wu, H.; Rota, R.; Morbidelli, M.; Varma, A. Parametric Sensitivity in Fixed-Bed Catalytic Reactors with Reverse-Flow Operation. *Chem. Eng. Sci.* **1999**, *54* (20), 4579–4588.
- (12) Henning, G. P.; Perez, G. A. Parametric Sensitivity in Fixed-Bed Catalytic Reactors. *Chem. Eng. Sci.* **1986**, *41* (1), 83–88.
- (13) Strozzi, F.; Zaldivar, J. A General Method for Assessing the Thermal Stability of Batch Chemical Reactors by Sensitivity Calculation Based on Lyapunov Exponents. *Chem. Eng. Sci.* **1994**, *49* (16), 2681–2688.
- (14) Strozzi, F.; Alo, M.; Zaldi, J. A Method for Assessing Thermal Stability of Batch Reactors by Sensitivity Calculation Based on Lyapunov Exponents: Experimental Verification. *Chem. Eng. Sci.* **1994**, *49* (24), 5549–5561.
- (15) Alos, M.; Strozzi, F.; Zaldivar, J. A New Method for Assessing the Thermal Stability of Semibatch Processes Based on Lyapunov Exponents. *Chem. Eng. Sci.* **1996**, *51* (11), 3089–3094.
- (16) Zaldivar, J.; Cano, J.; Alos, M.; Sempere, J.; Nomen, R.; Lister, D.; Maschio, G.; Obertopp, T.; Gilles, E.; Bosch, J.; Strozzi, F. A General Criterion to Define Runaway Limits in Chemical Reactors. *Journal of Loss Prevention in the Process Industries* **2003**, *16* (3), 187–200.
- (17) Bosch, J.; Strozzi, F.; Zbilut, J.; Zaldivar, J. On-line Runaway Detection in Isoperibolic Batch and Semibatch Reactors Using the Divergence Criterion. *Comput. Chem. Eng.* **2004**, *28* (4), 527–544.
- (18) Varma, A.; Morbidelli, M.; Wu, H. *Parametric Sensitivity in Chemical Systems*; Cambridge University Press, 1999.
- (19) Adrover, A.; Creta, F.; Giona, M.; Valorani, M. Explosion Limits and Runaway Criteria: a Stretching-Based Approach. *Chem. Eng. Sci.* **2007**, *62* (4), 1171–1183.
- (20) Jiang, F.; Cai, J.; Liu, B.; Xu, Y.; Liu, X. Particle Size Effects in the Selective Hydrogenation of Cinnamaldehyde over Supported Palladium Catalysts. *RSC Adv.* **2016**, *6*, 75541–75551.
- (21) Kummer, A.; Varga, T. Completion of Thermal Runaway Criteria: Two New Criteria to Define Runaway Limits. *Chem. Eng. Sci.* **2019**, *196*, 277–290.
- (22) Kummer, A.; Varga, T.; Abonyi, J. Genetic Programming-Based Development of Thermal Runaway Criteria. *Comput. Chem. Eng.* **2019**, *131*, No. 106582.
- (23) Goldsmith, B. R.; Esterhuizen, J.; Liu, J.-X.; Bartel, C. J.; Sutton, C. Machine Learning for Heterogeneous Catalyst Design and Discovery. *AIChE J.* **2018**, *64* (7), 2311–2323.
- (24) Spellings, M.; Glotzer, S. C. Machine Learning for Crystal Identification and Discovery. *AIChE J.* **2018**, *64* (6), 2198–2206.
- (25) Jirasek, F.; Alves, R. A. S.; Damay, J.; Vandermeulen, R. A.; Bamler, R.; Bortz, M.; Mandt, S.; Kloft, M.; Hasse, H. Machine Learning in Thermodynamics: Prediction of Activity Coefficients by Matrix Completion. *J. Phys. Chem. Lett.* **2020**, *11* (3), 981–985.
- (26) Onel, M.; Kieslich, C. A.; Pistikopoulos, E. N. A Nonlinear Support Vector Machine-Based Feature Selection Approach for Fault Detection and Diagnosis: Application to the Tennessee Eastman Process. *AIChE J.* **2019**, *65* (3), 992–1005.
- (27) Varga, T.; Szeifert, F.; Abonyi, J. Decision Tree and First-Principles Model-Based Approach for Reactor Runaway Analysis and Forecasting. *Engineering Applications of Artificial Intelligence* **2009**, *22* (4), 569–578.
- (28) Hu, W.; Knight, D.; Lowry, B.; Varma, A. Selective Oxidation of Glycerol to Dihydroxyacetone over Pt-Bi/C Catalyst: Optimization of Catalyst and Reaction Conditions. *Ind. Eng. Chem. Res.* **2010**, *49* (21), 10876–10882.
- (29) Xiao, Y.; Greeley, J.; Varma, A.; Zhao, Z. J.; Xiao, G. An Experimental and Theoretical Study of Glycerol Oxidation to 1,3-Dihydroxyacetone over Bimetallic Pt-Bi Catalysts. *AIChE J.* **2017**, *63* (2), 705–715.
- (30) Xiao, Y.; Varma, A. Catalytic Deoxygenation of Guaiacol Using Methane. *ACS Sustainable Chem. Eng.* **2015**, *3* (11), 2606–2610.
- (31) Xiao, Y.; Varma, A. Kinetics of Guaiacol Deoxygenation Using Methane over the Pt-Bi Catalyst. *Reaction Chemistry & Engineering* **2017**, *2* (1), 36–43.
- (32) Xiao, Y.; Varma, A. Highly Selective Nonoxidative Coupling of Methane over Pt-Bi Bimetallic Catalysts. *ACS Catal.* **2018**, *8* (4), 2735–2740.
- (33) Haldar, R.; Rao, D. P. Experimental Studies on Parametric Sensitivity of a Batch Reactor. *Chem. Eng. Technol.* **1992**, *15* (1), 34–38.
- (34) Xiao, Y.; Wang, Y.; Varma, A. Low-Temperature Selective Oxidation of Methanol over Pt-Bi Bimetallic Catalysts. *J. Catal.* **2018**, *363*, 144–153.
- (35) Aly, F. A.; Lee, L. L. Self-consistent Equations for Calculating the Ideal Gas Heat Capacity, Enthalpy, and Entropy. *Fluid Phase Equilib.* **1981**, *6* (3), 169–179.
- (36) Froment, G. F.; Bischoff, K. B. *Chemical Reactor Analysis and Design*; John Wiley & Sons, Inc., 1990; pp 403–406.
- (37) Antolini, E.; Salgado, J. R.; Gonzalez, E. R. The Stability of Pt-M (M = First Row Transition Metal) Alloy Catalysts and Its Effect on the Activity in Low Temperature Fuel Cells: a Literature Review and Tests on a Pt-Co Catalyst. *J. Power Sources* **2006**, *160* (2), 957–968.
- (38) Fischer, C.; Thede, R.; Baumann, W.; Drexler, H. J.; König, A.; Heller, D. Investigations Into Metal Leaching from Polystyrene-Supported Rhodium Catalysts. *ChemCatChem* **2016**, *8* (2), 352–356.
- (39) Wu, Z.; Wegener, E. C.; Tseng, H. T.; Gallagher, J. R.; Harris, J. W.; Diaz, R. E.; Ren, Y.; Ribeiro, F. H.; Miller, J. T. Pd-In Intermetallic Alloy Nanoparticles: Highly Selective Ethane Dehydrogenation Catalysts. *Catalysis Science & Technology* **2016**, *6*, 6965–6976.
- (40) Xiao, Y.; Varma, A. Conversion of Glycerol to Hydrocarbon Fuels via Bifunctional Catalysts. *ACS Energy Letters* **2016**, *1* (5), 963–968.
- (41) Bergeret, G.; Gallezot, P. Particle Size and Dispersion Measurements. *Handbook of Heterogeneous Catalysis*; Wiley, 2008; Vol. 1, pp 738–765.

(42) Weisz, P.; Prater, C. Interpretation of Measurements in Experimental Catalysis. *Adv. Catal.* **1954**, *6*, 143–196.



CAS BIOFINDER DISCOVERY PLATFORM™

# PRECISION DATA FOR FASTER DRUG DISCOVERY

CAS BioFinder helps you identify  
targets, biomarkers, and pathways

Unlock insights

**CAS**  
A division of the  
American Chemical Society